HIGH STRAIN RATE INTERLAMINAR TENSILE PROPERTIES OF FIBRE-REINFORCED POLYMER COMPOSITES USING A NOVEL IMAGE-BASED INERTIAL IMPACT (IBII) TEST

J. Van Blitterswyk[1], L. Fletcher[1] and F. Pierron[1]

[1]Mechanical Engineering, University of Southampton, Southampton SO17 1BJ, UK
Email: j.van-blitterswyk@soton.ac.uk

Keywords: high strain rate, interlaminar tension, fibre-reinforced polymer composites, dynamic test methods, ultra-high speed imaging, Virtual Fields Method

Abstract
This paper presents the design and experimental validation of a novel image-based inertial impact (IBII) test to measure the interlaminar tensile stiffness and strength of fibre-reinforced polymer composite materials at high strain rates. Ultra-high-speed imaging is combined with full-field measurements to measure and exploit the inertial effects generated under high strain rate loading. The virtual fields method is used to process the kinematic fields to directly identify interlaminar tensile stiffness and strength from maps of acceleration and strain. By doing so, the specimen acts like a dynamic load cell without having to grip the specimen or measure external force. This test was successfully used to measure the interlaminar stiffness and tensile strength on a carbon/epoxy pre-preg laminate at average, peak strain rates on the order 4,000 s^{-1}. Results show an increase in interlaminar stiffness and strength of approximately 30% and 129% compared to quasi-static values, respectively.

1. Introduction

Fibre-reinforced polymer (FRP) composite structures are increasingly used in applications subjective to dynamic loading (*e.g.*: impact, blast, crash, *etc.*). A thorough understanding of the constitutive behaviour over a wide range of strain rates must be established in order to use numerical simulations for modelling and design of composite structures subjected to these loading cases. Interlaminar properties are matrix-dominated, and should exhibit a strain rate dependency [1, 2]. However, the studies attempting to measure high strain rate properties in the interlaminar direction are relatively scarce and inconsistent [1]. Variations in material composition (fibre and matrix materials, fibre volume fraction, reinforcement architecture), contribute to this scatter, however, the key source the inconsistency primarily stems from limitations inherent to existing experimental techniques (*i.e:* high-speed load frames, Split-Hopkinson pressure bar, *etc.*)[1]. At high strain rates, inertial effects unavoidably induce heterogeneous kinematic fields and cause difficulty when attempting to make use of a few point measurements to infer the response of the material. This is particularly problematic for testing materials with low wave speeds, and low strengths, such as the interlaminar direction of FRP composites. As a result, achievable strain rates must be restricted to a few hundred s^{-1} in tension to reliably measure material properties with existing techniques.

This work presents the numerical design and experimental validation of a novel image-based inertial impact test (IBII) to obtain interlaminar tensile properties. Ultra-high-speed imaging, combined with the grid method, is used to measure full-field maps of acceleration and strain with sub-microsecond resolution. The maps are processed using the virtual fields method (VFM) to directly identify the

interlaminar stiffness parameters. The interlaminar tensile strength is also estimated using the VFM by reconstructing stress averages from acceleration fields. In this way, the specimen acts like a dynamic load cell, thus no external force measurement is required. The rest of the paper describes the test design, processing techniques, implementation of the test, and experimental measurements of interlaminar stiffness and tensile strength for a unidirectional carbon/epoxy laminate (AS4-145/MTM 45-1).

2. Test Concept

The proposed test configuration (Fig. 1) is designed to indirectly load the specimen in tension through the application of a compressive pulse from a projectile traveling at speed V_P. The specimen is bonded to the end of a `waveguide', which reduces non-uniformities in the kinematic fields measured on the specimen due to slight misalignments at impact. The pulse imparted by the projectile travels through the waveguide and is transferred into the specimen. Once in the specimen the pulse travels to the free edge, where it then reflects as a tensile wave travelling back towards the waveguide. For materials with higher compressive strength, the parameters of the projectile and waveguide can be tailored to ensure the reflected tensile pulse causes failure in the specimen.
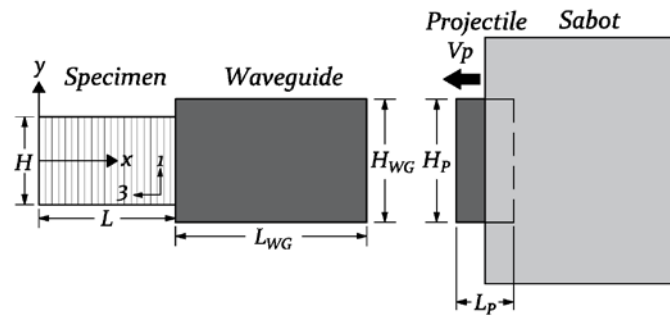
Figure 1. Schematic of IBII test configuration for interlaminar specimens [3].

Ultra-high speed imaging is combined with the grid method to measure dynamic displacement fields on the surface of the specimen. These maps encode the constitutive response of the material, which is extracted using the VFM. The initial compressive loading is used to identify the interlaminar stiffness using reconstructed stress-strain curves and optimized piece-wise virtual fields. The linear stress-gauge equation is used to estimate tensile strength. These identification procedures will be discussed in the next section.

3. The Virtual Fields Method (VFM)

The principle of virtual work is used to derive independent expressions relating the internal state of stress to external forces and acceleration. Through careful selection of virtual fields, substitution of an appropriate constitutive model, and using measured full-field maps of strain and acceleration, these expressions can be used for direct identification of the unknown constitutive parameters. In this work, the following assumptions are made: 1) constant, density, thickness and stiffness in space; 2) kinematic fields are uniform in the thickness dimension of the sample; 3) the specimen can be considered to be in a state of plane stress; and 4) neglect body forces. Under these conditions, the principle of virtual work has the following form:

$$-\int_S \boldsymbol{\sigma}:\boldsymbol{\epsilon}^* \, dS + \int_{\delta l} \overline{\boldsymbol{T}} \cdot \boldsymbol{u}^* \, dl = \rho \int_S \boldsymbol{a} \cdot \boldsymbol{u}^* dS \qquad (1)$$

J. Van Blitterswyk, L. Fletcher and F. Pierron

where S denote the volume and surface of the region of interest, $\overline{T}$ is the Cauchy stress vector acting along the in-plane boundary of the specimen δl, $\boldsymbol{u}^*$ is the virtual displacement field, $\boldsymbol{\epsilon}^*$ the virtual strain field, $\boldsymbol{a}$ is the acceleration field, and $\boldsymbol{\sigma}$ the Cauchy stress tensor. Note that : and $\cdot$ denote the dot product in matrix and vector forms, respectively. The first and second terms on the left hand side of Eq. (1) represent the internal and external virtual work, respectively. The term on the right hand side of the equation represents the virtual work of inertial forces.

3.1   Stiffness identification

The 'stress-gauge' equation is derived from Eq. (1) by substituting in rigid-body virtual fields ($u_x^* = 1$, $u_y^* = 0$). This relates the average axial stress, $\overline{\sigma_{xx}}^y$, at any position, x_o, and time, t, to measured surface accelerations (Eq. (2)):

$$\overline{\sigma_{xx}}^y = \rho x_0 \overline{a_x}^S \tag{2}$$

where superscript y coupled with an overline denotes the width average at x_o, and superscript S coupled with an overline denotes the surface average between the free edge and x_0. Stress averages are reconstructed at each cross-section using the stress-gauge equation [3,4]. The average stress, $\overline{\sigma_{xx}}^y$ is plotted against average strain, $\overline{\varepsilon_{xx}}^y$ to generate stress-strain curves from which the interlaminar stiffness is identified. This is used to verify the linearity of the response and spatial uniformity of the stiffness. Special optimised virtual fields have also been adopted for direct stiffness identification, as developed in [5]. Specifically, a reduced formulation is adopted using a uniaxial virtual strain field and neglecting transverse strains from very small Poisson effect. This enables E_{33} to be identified directly as outlined in [3,4].

3.2   Strength identification

A linear approximation for the stress distribution across the width of the specimen may be reconstructed by considering additional rigid-body virtual fields ($u_x^* = 0$, $u_y^* = 1$; $u_x^* = y$, $u_y^* = -x$). This is referred to as the 'linear stress-gauge' (LSG) approach (Eq. (3)).

$$\sigma_{xx}(LSG) = \rho x_o \overline{a_x}^S + \frac{12\rho x_0 y}{H^2}(\overline{a_x}y^S - \overline{a_y x}^S + x_0\overline{a_y}^S) \tag{3}$$

In Eq. (3) H denotes the total specimen width. It is important to note that the linear stress-gauge equation does not full resolve σ_{xx} across the width of the specimen, and only provides a linear approximation to the stress at any given position on the specimen. It is also important to highlight that both stress-gauge equations are valid regardless of the constitutive behaviour. In this work, the linear stress-gauge equation is used to estimate the tensile strength at the crack location since it accounts for possible asymmetry in the stress field.

4.   Test Design

The material used in this study is a unidirection carbon/epoxy composites, AS4-145/MTM45-1. The length of the specimen was fixed at the nominal plate thickness of 18 mm. The 1-3 interlaminar plane was the focus of this study (*e.g.:* fibres perpendicular to the direction of impact (Fig. 1)). A height of 12 mm was selected to maximise the spatial resolution of the Shimadzu HPV-X camera (400 x 250 pixels) used to image the specimens. An additional 2 mm at the free edge was considered when selecting the height dimension to account for rigid-body displacement. A thicker laminate is considered here for simplicity as it enables plate-like specimens to be machined, and accurate grids to be deposited for full-field measurement purposes. The height of the waveguide (H_{WG}) and projectile (H_P) was fixed at 25 mm. Both were machined from Al 6061-T6. Having a larger waveguide and projectile makes

alignment easier and a separate numerical study showed that the impactor height has minimal influence so long as it does not exceed three times the height of the sample. The projectile is embedded in a Nylon 6-6 sabot, with a height equal to that of the diameter of the gas gun (50 mm). Details about the gas-gun apparatus can be found in [4].

Projectile length and impact speed were selected using a design sweep based on simulated experiments with ABAQUS/Explicit. Parameters were chosen such that: 1) the impact induced at least 100 MPa of tensile stress and 2) the geometry maximised the reflected stress ratio (*i.e.*: reduces the required compressive stress to avoid damaging the specimen). The simulations were parameterized such that projectile length and impact velocity could be systematically varied. From each simulation, the maximum tensile stress was extracted to identify a range of parameters which would satisfy both requirements. Since the waveguide and projectile are made of the same material, the waveguide length must be at least twice the length of the projectile to avoid clipping the pulse. For all simulations the waveguide length, L_{WG}, was fixed at 50 mm. Based on the design sweep the following experimental parameters were selected: $L_P = 10$ mm, $V_P = 50$ m·s^{-1}.

5. Experimental setup

All tests were performed using the compressed air impact rig described in [4]. Each specimen was bonded to the back of a 6061-T6 aluminium waveguide (50 mm length, 25 mm diameter) using a thin layer of cyanoacrylate glue. A copper contact trigger on the front of the waveguide was used to trigger the camera. A 10 µs delay was programmed between the trigger event and image capture to account for the traverse time of the wave through the waveguide. All images were captured using the Shimadzu HPV-X camera (frame rate = 5 Mfps) with a Sigma 105 macro lens. The optical setup and a mounted specimen are shown in Figs. 2a and 2b, respectively. Grids with a pitch p of 0.3 mm were bonded to five specimens, using the process outlined in [29] ('-B[1-3]' appended after specimen number). A second grid deposition process was explored for the remaining five specimens. A thin coat of white rubber paint (Rust-Oleum Peel Coat) was first applied to the specimen. A series of black squares with an average pitch of 0.337 mm were then printed onto the painted surface with a Canon Océ Arizona 1260 XT flat bed printer ('-P[1-3]' appended after specimen number). Full details about the test setup can be found in [3].
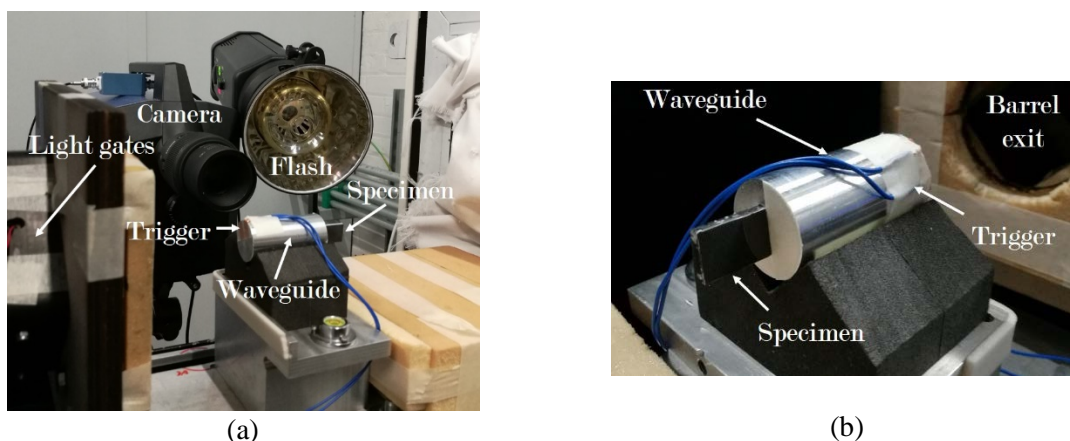
Figure 2. Experimental setup used for all interlaminar tests: (a) camera and ash arrangement around the test chamber, and (b) a mounted specimen supported on a test stand in the test chamber [3].

6. Results

To validate the proposed test, ten specimens were cut such that the fibres were perpendicular to the direction of impact (1-3 plane). Example stress-strain curves reconstructed for two interlaminar

specimens are shown in Fig. 3. Stress-strain curves were reconstructed at cross-sections along the length of the specimen, with the average over the middle of the specimen taken as the identified stiffness value.
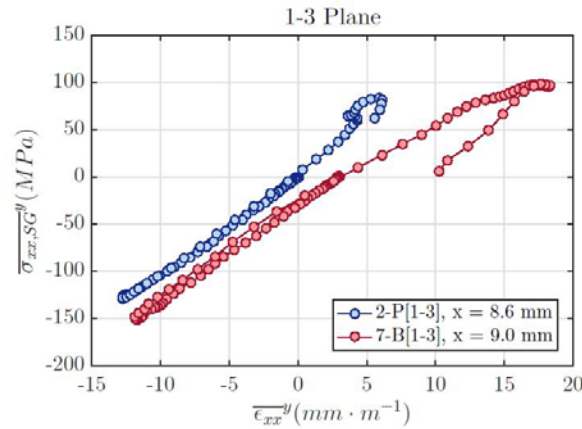
Figure 3. Sample stress-strain curves for two samples using the stress-gauge equation (Eq. (2)) [3].

The linear stress gauge equation (Eq. (3)) was used to estimate tensile strength. The fracture location was identified in the raw strain fields as shown in Fig. 4a. The interlaminar tensile strength was taken as the maximum stress over time within a gauge region of 2 pitches x 4 pitches (x,y) centered on the fracture location (black rectangle in Fig. 4a). An example of the stress-strain response within the gauge region is shown in Fig. 4b. A summary of measured interlaminar stiffness and tensile strength are listed in Table 1.

(a)   (b)
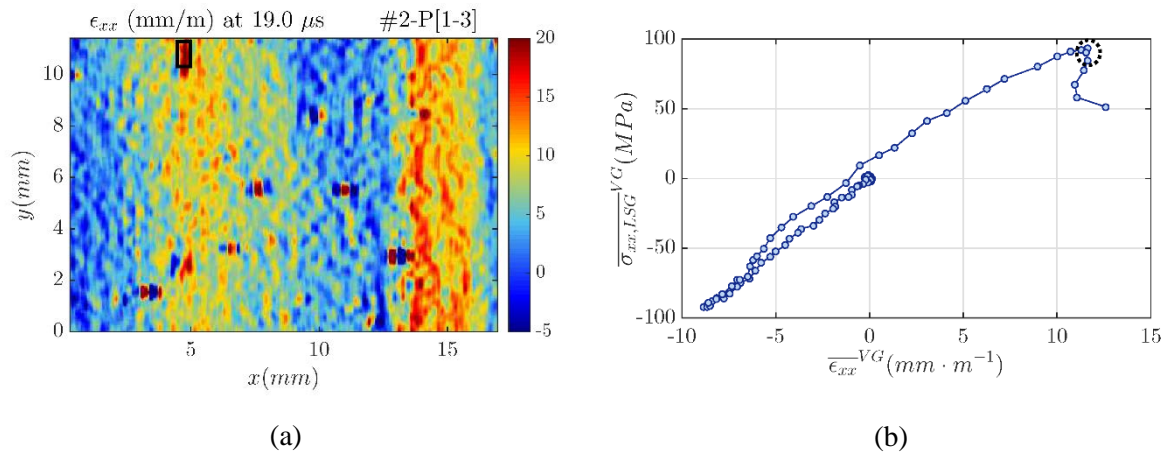
Figure 4. Strength identification diagnostics for specimen #2-P[1-3]. (a) raw, un-smoothed ε_{xx} strain field (mm·m-1), and (b) stress-strain curve generated using average σ_{xx}(LSG) and ε_{xx} within the virtual gauge region (superscript 'VG'). In (a) the virtual gauge is shown as the black rectangle. In (b) the dashed circle indicates the point of fracture and extracted strength using the linear stress-gauge equation [3].

Table 1. Summary of measured interlaminar strength and stiffness

Specimen	Stress-Gauge		Optimised VFM	Quasi-Static [6]	
	E_{33} [GPa]	$\sigma_{33}{}^{ult}$ [MPa]	E_{33} [GPa]	E_{33} [GPa]	$\sigma_{33}{}^{ult}$
1-3 plane	10.32 ± 0.34	115.2 ± 24.2	10.38 ± 0.39	7.9	28.9 - 50.3

The interlaminar stiffness measurements show good consistency with both identification approaches. The average measured stiffness represents and increase of approximately 30 % compared to quasi-static

values. Tensile strength shows a greater strain rate sensitivity with the average value of 115 MPa representing an increase of 129% compared to quasi-static measurements. using in the measurement of strength and stiffness. Assigning a single strain rate value to the measured properties is challenging as the inertial effects create highly heterogeneous strain and strain rate maps. However, when axial strain is high, so too is strain rate and therefore, the peak, width-average strain rate can be considered as an 'effective' strain rate for these measurements (on the order of 4,000 s^{-1}). Reliable measurement of stiffness and strength at these strain rates is not possible using existing test methods. Relative to quasi-static values, the stiffness increases by approximately 30 %, and strength by 135 %.

7. Conclusions

A novel image-based inertial impact test to measure the interlaminar tensile stiffness and strength has been successfully designed and validated. Interlaminar stiffness and tensile strength were successfully measured at strain rates where current techniques are unreliable (on the order of 4,000 s^{-1}). Combining ultra-high speed, full-field measurements with the virtual fields method enables many of the limitations associated with existing techniques to be removed and opens the way for the next generation of high strain rate tests. Future work includes the extension of the IBII test concept to combined tension and shear loading to begin populating more complete failure envelopes at high strain rates. This information is not currently available and is required for improved high strain rate modelling of composite materials.

References

[1]   R. Gerlach, C. R. Siviour, N. Petrinic, and J. Wiegand. *Experimental characterisation and constitutive modelling of RTM-6 resin under impact loading*. Polymer, 49(11):2728-2737, 2008.

[2]   J. Van Blitterswyk, L. Fletcher, and F. Pierron. *Characterisation of the interlaminar properties of composites at high strain rates: a review*. Advanced Experimental Mechanics, 2(June):3-28, 2017.

[3]   J. Van Blitterswyk, L. Fletcher, and F. Pierron. *Image-based inertial impact test for composite interlaminar tensile properties*. Submitted to Journal of Dynamic Behavior of Materials, 2018.

[4]   L. Fletcher, J. Van Blitterswyk, and F. Pierron. *A novel image-based inertial impact (IBII) test for the transverse properties of unidirectional composites at high strain rates*. Submitted to Composites Part A, 2017.

[5]   S. Avril, M. Grédiac, and F. Pierron. *Sensitivity of the virtual fields method to noisy data*. ComputationalMech, 34:439-451, 2004.

[6]   E. Clarkson, T. Valliappan, and D. Tan. CYTEC (Formerly Advanced Composites Group) *MTM45-1/ 12K AS4 45gsm 32%RW Unidirectional Qualification Statistical Analysis Report FAA Special Project Number SP3505WI-Q Test Panel Fabrication Facility*. Technical report, National Institute for Aerospace Research (NIAR), Tulse, OK, 2016.